J. Fluid Mech. (1991), *vol.* 233, *pp.* 119–139
Printed in Great Britain

Propagation of barotropic vortices over topography in a rotating tank

By G. F. CARNEVALE[1], R. C. KLOOSTERZIEL[2]
AND G. J. F. VAN HEIJST[3]

[1] Scripps Institute of Oceanography, University of California, San Diego, La Jolla, CA 92093, USA

[2] Institute for Nonlinear Science (INLS), University of California, San Diego, La Jolla, CA 92093, USA

[3] Department of Technical Physics, Eindhoven University of Technology, 5600 MB Eindhoven, The Netherlands

(Received 24 April 1990 and in revised form 10 May 1991)

A small-scale cyclonic vortex in a relatively broad valley tends to climb up and out of the valley in a cyclonic spiral about the centre, and when over a relatively broad hill it tends to climb toward the top in an anticyclonic spiral around the peak. This phenomenon is examined here through two-dimensional numerical simulations and rotating-tank experiments. The basic mechanism involved is shown to be the same as that which accounts for the northwest propagation of cyclones on a β-plane. This inviscid nonlinear effect is also shown to be responsible for the observed translationary motion of barotropic vortices in a free-surface rotating tank. The behaviour of isolated vortices is contrasted with that of vortices with non-vanishing circulation.

1. Introduction

Investigations into the propagation of monopolar vortices on a β-plane (Adem 1956; McWilliams & Flierl 1979; Mied & Lindemann 1979; among others) have clearly established that in the northern hemisphere, the initial tendency for a cyclone is to propagate to the northwest. In as much as the role of layer-thickness variations is similar in effect to spatial variations of rotation rate (i.e. the β-effect), at least to quasi-geostrophic order, one can deduce a rule of 'local northwest' propagation of cyclones relative to contours of topography. If the horizontal scale of a vortex is much smaller than that of the topography over which it lies, then one can model the topography locally by a constant slope and, relative to the direction of this slope, define local compass directions. Thus by the same mechanism that makes the cyclonic vortex move toward the northwest on a β-plane, a cyclone over broad topography is at any instant expected to propagate toward the local northwest (i.e. upslope and toward the left). Thus, a cyclone would climb up out of a valley in a cyclonic spiral around the centre, and climb up the slope of a hill in an anticyclonic spiral around the peak (see Carnevale *et al.* 1988). The 'local northwest' propagation rule cannot apply when the scale of the vortex is much larger than that of the hill. In that case, the theory of large-scale flow over topography applies with the vortex acting solely as a large-scale velocity field. The main feature of that phenomenon is the creation of an anticyclone over the hill and a cyclone just off the hill (cf. Huppert & Bryan 1976; Carnevale *et al.* 1988). In the intermediate regime, in which the horizontal scales of the hill and the vortex are comparable, numerical simulations reveal a scenario built of two limiting cases. The vortex then orbits the peak in a manner described below.

Symmetry implies that for anticyclones the rule is 'local southwest' propagation relative to the contours of topography. Thus an anticyclone will move downhill but also in an anticyclonic spiral relative to the centre of the hill. For the southern hemisphere (i.e. negative Coriolis parameter f), the terms northwest and southwest would need to be interchanged. However, the terms cyclonic and anticyclonic can be used without reference to the specific hemisphere (note that cyclonic implies counterclockwise/clockwise in the northern/southern hemisphere). Below we shall have a northern-hemisphere orientation in mind when speaking of northwest propagation.

The northwest propagation rule should hold for all cyclones. Here we investigate two very different types: isolated cyclones, which have no net integrated vorticity (i.e. zero circulation), and non-isolated ones, which have non-vanishing circulation. We use the term isolated to mean that the velocity distant from the centre of the vortex falls off faster than $1/r$. One can expect that the isolated vortices will not be influenced as much by boundary conditions as vortices of net circulation. We first examine the evolution of these vortices on a simple inclined plane in the rotating tank. Although both do indeed follow the northwest propagation rule, their paths are rather different. Further, the evolution of their structures, in particular with regard to the dispersal of passive dye tracer, are substantially different. The inclined-plane study is followed by a discussion of the propagation of these vortices over conical hills and valleys. Finally, the phenomenon of vortex motion under a free surface in a rotating tank is shown to be attributable to the topographic effect of the parabolic upper free surface. Through numerical simulations, we verify that the essential mechanism in all these cases is inviscid, quasi-geostrophic and barotropic.

2. Fundamental mechanisms

The numerical simulations which we shall describe are all based on the quasi-geostrophic equation for a single homogeneous layer:

$$\frac{\partial q}{\partial t}+\nabla\cdot(\boldsymbol{v}q)=0, \tag{1}$$

where $\boldsymbol{v}$ is a divergenceless velocity field, which can be written in terms of the stream function ψ according to

$$\boldsymbol{v}=(u,v)=\left(-\frac{\partial\psi}{\partial y},\frac{\partial\psi}{\partial x}\right). \tag{2}$$

Here the potential vorticity, q, is taken to be

$$q=\nabla^2\psi+h+\beta y, \tag{3}$$

where h is defined by

$$h(x,y)=f_0\frac{\Delta H}{D}, \tag{4}$$

with f_0 the Coriolis parameter, that is, twice the rotation rate, D the mean depth, and ΔH the height of the topography above the mean bottom.

The term β measures the spatial variation of the Coriolis parameter (i.e. $f=f_0+\beta y$). Equation (1) is equivalent to the conservation of q following particles, with the value of the relative vorticity ζ on the particle determined from its initial value of q and the value of the topography h at the current position. As a particle is advected, its relative vorticity changes in accordance with this conservation law. In turn the velocity field that this particle induces at some distant point can be determined by inverting the Laplacian in the relation $\zeta = \nabla^2\psi$, and using the definitions in (2). With respect to the laboratory experiments, a 'particle' is understood to be a Taylor column of infinitesimal cross-section. Thus, the evolution of barotropic two-dimensional flows is governed by the mutual advection of infinitely many continuously distributed point vortices that each conserve their potential vorticity q.

Basically we are interested in the evolution of a vortex of relatively small horizontal scale over a broad topographic feature. A first understanding of this interaction can be obtained by considering the extreme limit of topography of constant slope. The βy term in the evolution equation (1) plays the same role as a constant-slope topography. The β-plane problem has been widely studied both analytically and numerically (e.g. Adem 1956; McWilliams & Flierl 1979; Mied & Lindemann 1979), and also in conjunction with rotating-tank experiments (see Firing & Beardsley 1976; Takematsu & Kita 1988; Masuda, Marubayashi & Ishibashi 1990).

In absence of β, topography, and viscosity, a radially symmetric vortex is a stationary flow. If only linear radiation is allowed, that is, if the nonlinear evolution equation is replaced by the linear Rossby wave equation

$$\frac{\partial\zeta}{\partial t} = -\beta\frac{\partial\psi}{\partial x}, \tag{5}$$

then monopolar vortices radiate non-interacting, linear Rossby waves, and the peak of the vorticity field moves due west. In fact, one of the earliest papers concerning the motion of vortices on a β-plane (Bjerkness & Holmboe 1944) predicted a westward translation. Flierl (1977) addressed the initial-value problem of a vortex with Gaussian stream function $\psi \sim \exp(-\frac{1}{2}r^2)$ on an infinite domain. By showing that the so-called Bessel eddies, which have stream function proportional to an ordinary zero-order Bessel function, travel steadily westward with a speed depending on their spatial scale (as previously noted by Tojo 1953), and decomposing the eddy by Fourier–Bessel transform, it can be deduced that the centre of an isolated eddy moves westward under the purely linear dynamics. However, the eddy rapidly disperses because its energy is radiated away by Rossby waves. Similar conclusions were arrived at by Firing & Beardsley (1976) who considered the initial-value problem of an isolated vortex initially in the centre of a closed circular domain. On periodic domains, the linear dynamics lead to the same behaviour (see Chan & Williams 1987). In all these cases, the Rossby wave radiation wake is symmetric about the east–west axis, as it must be from symmetry considerations – equation (5) as well as the initial and boundary conditions are invariant under the mapping $y \rightarrow -y$.

Under the full nonlinear evolution equations the behaviour is more complicated. In an analytical study of the barotropic vorticity equation on a β-plane, Adem (1956) showed by means of a Taylor series expansion in time that to lowest order in β the $O(t)$ term in the expansion (corresponding to the linear dynamics) predicts a westward shift of an isolated cyclone, whereas the $O(t^2)$ term adds a northward component to it, the latter being a truly nonlinear effect. Such a tendency to move northward was pointed out by Rossby (1948) who showed that the average Coriolis force acting on a monopole is directed to the north for a cyclone. By combining these two lowest-order terms, it was concluded by Adem (1956) that the initial tendency of an isolated cyclone on a β-plane would be to propagate to the northwest. Since the barotropic vorticity equation is invariant under the mapping $\{\psi, y\} \rightarrow \{-\psi, -y\}$, it would thus follow that an anticyclone on a β-plane propagates to the southwest. There has been some criticism of Adem's line of reasoning (see Willoughby 1988), but simulations of the full nonlinear equations (McWilliams & Flierl 1979; Mied & Lindemann 1959; Chan & Williams 1987; Carnevale *et al.* 1988; Masuda *et al.* 1990) not only show that this initial tendency is obeyed, but also that the overall tendency for many eddy turn-over times of the primary vortex is toward the northwest, although the trajectory may become somewhat complicated. An important feature of the nonlinear evolution that distinguishes it from the linear evolution is that the energy remains fairly localized if the eddy is sufficiently nonlinear, and as such it is a coherent nonlinear entity, recognizable over long periods. Carr & Williams (1989) have performed a study of the mechanisms accounting for the dispersion-resistant properties of vortices on a β-plane. Similar results are found in the laboratory experiments that will be described below. Speed and direction have been found to depend on amplitude and spatial extent of an isolated vortex (see McWilliams & Flierl 1979; Mied & Lindemann 1979; Chan & Williams 1987). In the present study we contrast the behaviour of an isolated vortex with that of a non-isolated vortex. We find that although both kinds do show propagation to the local northwest, there are important differences in their trajectories and the evolution of their structure.

Observation of the vorticity fields in the numerical simulations suggest that the mechanism behind this tendency to move northwestward is the early evolution of a dipolar perturbation field on the initial monopolar structure. This comes about by the cyclonic advection of fluid around the central core and the conservation of potential vorticity on the advected fluid. Particles to the east of the core moving northward must decrease their relative vorticity while those to the west of the core moving southward increase their relative vorticity. Owing to the radial symmetry of the initial velocity field this generation of vorticity anomaly results in a distortion of the shape of the initial vortex that can be described as a dipolar perturbation vorticity field with its axis oriented toward the northwest. The whole structure is then carried toward the northwest by the velocity field induced by this dipolar perturbation. The precise angle of the trajectory depends on the structure of the initial vorticity distribution. After this initial phase, the motion can be more complicated as satellite vortices are created and possibly shed (see §3.1).

3. Rotating-tank experiments

To test the predictions of the numerical simulations, we performed a series of rotating-tank experiments. The tank has a diameter of 92.5 cm. The level of water in the experiments was 20 cm and the rotation rate (counterclockwise when seen from above) was adjusted to a period of either 6.1 s or 10.4 s. This corresponds to a rotation rate of the table of approximately $\Omega = 1 \text{ rad s}^{-1}$ and $\Omega = 0.6 \text{ rad s}^{-1}$ respectively. The upper surface was left free, and various topographies were used on the bottom of the tank. After the fluid has spun-up to solid-body rotation, the free surface assumes a parabolic profile, which can be represented in the quasi-geostrophic equations by an ambient potential vorticity,

$$h = -\frac{f_0^3 R^2}{8gD}, \tag{6}$$

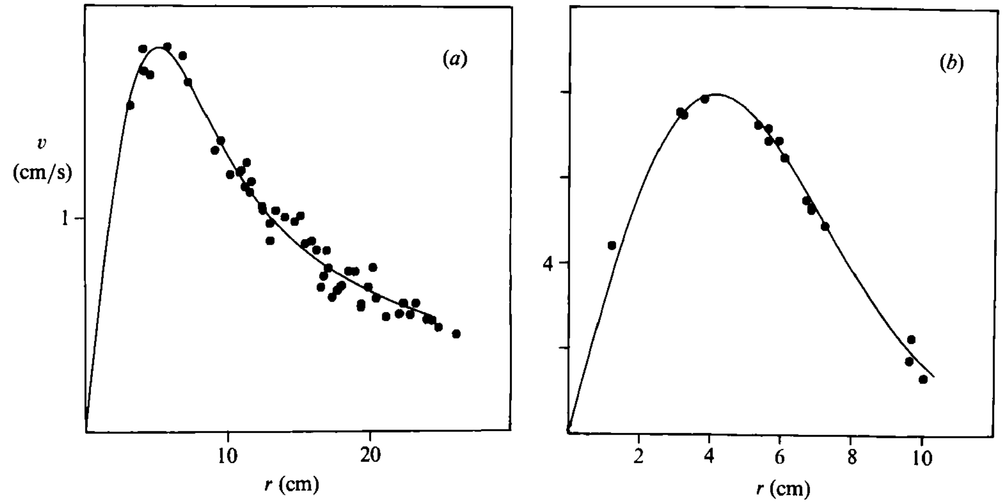

FIGURE 1. Graphs showing the radial distribution of azimuthal velocity of (*a*) a sink vortex with $\mu \approx 4\ \mathrm{s}^{-1}$ and $\sigma \approx 3.5$ cm, and (*b*) a typical stirred vortex of vorticity amplitude $\mu \approx 6\ \mathrm{s}^{-1}$ and horizontal scale $\sigma \approx 4$ cm. Measured velocities are indicated with black dots while the solid lines are the ideal profiles given by equations (7) and (9).

where R is the horizontal distance of a point from the centre of the tank and $f_0 \equiv 2\Omega$. The topographic features that we examine here all have slopes considerably greater than that of the free surface, thus making the effect of the free-surface curvature negligible in comparison to the bottom topography. However, the case of flow on a flat bottom under this free surface has also proved very interesting (see §3.4).

The experiments were initialized by the creation of cyclonic vortices. The vortices are readily created by either stirring or by suction. In the suction method, water is siphoned from the bottom of the tank. In the stirring method, a bottomless cylinder of small diameter is placed in the tank and the fluid confined within is stirred until a vortex is formed. Then the cylinder is removed from the tank, leaving behind an isolated cyclone. In some experiments the fluid in the vortices was dyed. After a period of adjustment, the two-dimensionality of the flow was evident in that the sheets of dye in the fluid were vertical as in well-formed Taylor columns. A record of the evolution of the flow was kept by photographing tracer particles on the free surface. Laboratory experiments with anticyclonic vortices are not discussed in this paper because special care is needed to generate anticyclones since, unless they have Rossby numbers well-below $O(1)$, they are centrifugally unstable (see Kloosterziel & van Heijst 1991).

Sink vortices were created by inserting a tube of a small diameter ($\sim$ 2 cm) into the tank and siphoning a fixed amount of water at the bottom. On a flat bottom, after a short adjustment period, the resulting vortex typically has an azimuthal velocity distribution as shown in figure 1 (*a*) The data points are approximated by the solid curve given by

$$v_{\mathrm{sink}}(r) = (\sigma^2\mu/r)\,(1-\exp(-r^2/2\sigma^2)). \tag{7}$$

The corresponding vorticity field for this profile is

$$\zeta_{\mathrm{sink}}(r) = \mu\exp(-r^2/2\sigma^2). \tag{8}$$

Here μ is the peak vorticity strength, σ the horizontal lengthscale, and r the distance from the centre of the vortex. Note that this vorticity distribution is single signed, as opposed to the vorticity distribution of a stirred vortex, and that the sink vortex has non-vanishing circulation and thus is not isolated. Griffiths & Hopfinger (1987) noted that barotropic sink vortices are reasonably well described by the Rankine vortex model – which has a constant-vorticity core surrounded by potential ($1/r$) flow – but that in fact the vorticity varies in the core, and that the peak of the velocity is rounded near the radius of maximum velocity. The profile given by (8) has all these properties and is representative of the structure of the sink vortex shortly after the forcing has stopped.

A typical example of the measured, azimuthal velocity distribution of a stirred cyclonic vortex, on a flat bottom, is shown in figure 1 (*b*). The data points are fitted by the profile given by

$$v_{\text{stir}}(r) = \tfrac{1}{2}\mu r \exp\left(-r^2/2\sigma^2\right), \tag{9}$$

which is represented by the solid curve in figure 1 (*b*). The vorticity field implied by (9) is

$$\zeta_{\text{stir}}(r) = \mu(1-r^2/2\sigma^2)\exp\left(-r^2/2\sigma^2\right). \tag{10}$$

The Rossby numbers ϵ of the vortices typically used in the laboratory experiments are initially not small. Based on the peak velocity and a lengthscale L equal to the radius at which the peak velocity is found, i.e. $\epsilon \equiv v_{\max}/(\Omega r_{\max})$, initial Rossby numbers of typical laboratory vortices studied here are $O(1)$. For quasi-stationary, circularly-symmetric swirling flows with Rossby numbers of this magnitude, one has gradient–wind balance instead of geostrophy (see Holton 1979). However, owing to lateral diffusion of momentum and bottom drag by the Ekman layer in the laboratory, these vortices rapidly enter the geostrophic regime. Since the aspect ratio is $O(1)$, even for small Rossby numbers the validity of the quasi-geostrophic equations for laboratory vortices cannot be strictly justified on the basis of a scale analysis. Another point is that the topography used in the laboratory experiments is not truly shallow. However, as was noted by McWilliams, Gent & Norton (1986) and Mied & Lindemann (1979), in many cases the assumption of quasi-geostrophy for modelling purposes gives qualitatively satisfying results. We have used the quasi-geostrophic equations to model the processes observed in our rotating-tank experiments and as shown below the agreement can be very good. As a final point, it should be mentioned that in the numerical experiments the Rossby deformation radius was put equal to infinity ('rigid lid' approximation). The experimental parameters correspond to a Rossby deformation radius,

$$L_D = \frac{(gD)^{\frac{1}{2}}}{2\Omega}, \tag{11}$$

of 1 m for the low rotation rate, and 0.65 m for the high, taking the average depth over the topography as $D = 17.5$ cm. We neglect the finite-deformation-radius effect in the first approximation when considering phenomena with lengthscales of approximately 10–20 cm. Numerical experiments by Holloway, Riser & Ramsden (1986) indicate that neglect of this term, in our parameter range, will not significantly change the path of the vortex on the β-plane.

Once created the cyclones spin down at a rate which is well explained by the bottom drag due to Ekman pumping combined with lateral diffusion of momentum. The Ekman dynamics alone provide a rate of decay that is close to constant in the absence of any topography and is given approximately by the Ekman timescale

$$t_{\text{E}} = \frac{D}{(\nu\Omega)^{\frac{1}{2}}}, \tag{12}$$

which is incorporated into the quasi-geostrophic equations according to

$$\frac{\partial q}{\partial t}+\nabla\cdot(vq) = -\frac{1}{t_E}\zeta+\nu\nabla^2\zeta. \tag{13}$$

Note that this is the decay rate appropriate to a flat but stress-free surface and a flat bottom. In the case of a rigid, no-slip, upper surface the Ekman decay rate is doubled (cf. Pedlosky 1979). For the parameters of these experiments ($\nu = 0.013$ cm^{2}s^{-1}, $D \approx$ 15–20 cm, $\Omega = 0.6$, 1 rad s^{-1}, where ν is the molecular kinematic viscosity for water at 10 °C), this corresponds to an Ekman e-folding time of about 150 s for the high rotation rate and 200 s for the low, based on the average value $D = 17.5$ cm. The second term on the right-hand side of (13) represents the ordinary Laplacian diffusion of momentum. For the experimental regime investigated here Laplacian diffusion and Ekman damping have comparable effects on the amplitude decay of the vortex. This can be seen by directly comparing the timescales t_E and $t_\nu = \sigma^2/\nu$, which are of the same order of magnitude. Also, we can calculate the exact solutions of (13) including both these mechanisms for the flat-bottom problem. The evolution of vortices initially (at $t = 0$) given by (8) and (10), is found to be

$$\zeta_{\text{sink}}(r,t) = \frac{\mu e^{-t/t_E}}{(2\nu t/\sigma^2)+1}\exp\left\{\frac{-r^2}{2\sigma^2+4\nu t}\right\} \tag{14}$$

and

$$\zeta_{\text{stir}}(r,t) = \frac{\mu e^{-t/t_E}}{((2\nu t/\sigma^2)+1)^2}\left\{1-\frac{r^2}{2\sigma^2+4\nu t}\right\}\exp\left\{\frac{-r^2}{2\sigma^2+4\nu t}\right\} \tag{15}$$

(see Kloosterziel 1990). Consider the effect of linear decay after one Ekman period of, say, $t_E = 200$ s. The Ekman decay alone reduces the amplitude by a factor of $e^{-1} \approx$ 0.37. For the stirred vortex, with $\sigma \sim 2.5$ cm, the diffusion reduces the amplitude by an additional factor of about 0.37. For the sink vortex with $\sigma \sim 2.5$ cm diffusion introduces an additional factor of 0.7. Thus, in both cases, diffusion can add considerably to the rate at which the vortices decay during the first Ekman period, and cannot be neglected if a quantitative match between simulations and experiments is sought. The duration of the laboratory experiments varied from about half an Ekman period up to three times the Ekman period, depending on the initial strength and path of the vortex.

In what follows we compare our laboratory results with numerical simulations of equation (13). These are spectral simulations in a doubly periodic domain using the dealiased Fourier scheme of Patterson & Orszag (1972). The resolutions used correspond to grids with $N\times N$ points, with $N = 64$, 128 and 256, with fast Fourier transforms converting the configuration-space fields into the corresponding wave-vector amplitude description with the same number of variables. Questions of the adequacy of resolution for a particular case were checked by doubling N and rerunning the simulation. The influence of domain size over the course of an experiment was checked by performing the same numerical simulation with three different box sizes (50 × 50 cm, 100 × 100 cm and 200 × 200 cm), with the number of gridpoints per unit area held fixed.

3.1 *β-plane experiments*

We begin our discussion with the case of the behaviour of a cyclone on a β-plane. In the tank one does not have a position-dependent rotation rate; however, the β-effect can be mimicked by an inclined plane on the bottom of the tank, at least at the level

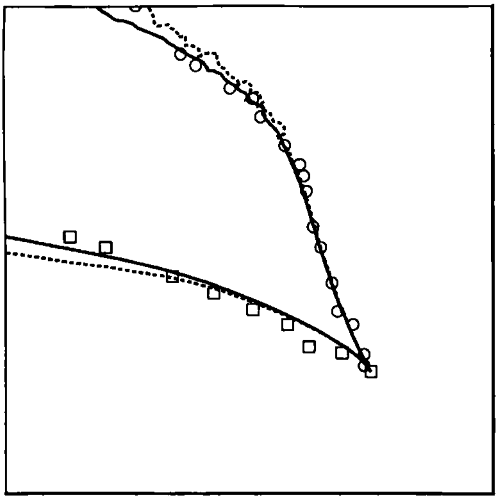

FIGURE 2. Graphs showing the trajectories of sink and stirred vortices on an inclined plane. The figure is oriented so that the shallowest end of the tank (i.e. the 'north' side) is at the top of the page. The vortices move from 'southeast' to 'northwest.' The positions of the laboratory sink (stirred) vortex are indicated by squares (circles). The data points for the sink vortex were taken at the following times after the cessation of forcing: 20, 25, 30, 35, 40, 45, 50, 60 and 65. The data points for the stirred vortex were taken at the following times after the removal of the cylinder in which the vortex was created: 7, 10, 15, 20, 25, 30, 35, 40, 45, 50, 55, 65, 70, 80, 90, 100 and 115 s. The solid (dashed) curves show the trajectories of the vortices in the corresponding viscous (inviscid) one-layer, quasi-geostrophic, numerical simulations. The duration of the trajectories shown for the viscous simulation for the sink (stirred) vortex is 54 (112) s, while for the inviscid simulation it is 53 (80) s. The computational domain size is 50 × 50 cm.

of quasi-geostrophic approximation, and the appropriate correspondence is deduced from equations (3) and (4). Here we use a plate 50 cm wide and 75 cm long. It was raised at one end of the tank to a height of 10 cm, giving the slope 10/75. This is represented in the quasi-geostrophic equations by an ambient potential vorticity $h = (f_0 s/D)y$, where s is the slope of the plane. In most experiments the vortices travelled over no more than half the plate towards the north, and thus we use 17.5 cm as the mean depth D in our calculations. In this section, we show experiments with the low rotation rate ($f_0 = 1.2\ \mathrm{s}^{-1}$) for which the effective β is 0.914 $10^{-2}\ \mathrm{cm}^{-1}\mathrm{s}^{-1}$.

The behaviour of both sink and stirred vortices over the inclined plane has been investigated. Figure 2 shows two typical trajectories: one for a sink vortex (squares) and one for a stirred vortex (circles). We also show the corresponding trajectories from numerical simulations of the viscous flow (solid lines) and the inviscid flow (dashed lines). The position of the vortex centre at consecutive moments has been determined from streakline photographs. The last shown data point for the sink (stirred) vortex trajectory was taken at 65 (115) s after the creation of the vortex. The latest points shown on the simulated viscous trajectories correspond to times 54 and 112 s for the sink and stirred vortex respectively. The initial strength and scale of the sink vortex for the simulation were estimated from the experiment streakline photographs as $\mu = 3.3\ \mathrm{s}^{-1}$ and $\sigma = 2.5$ cm (cf. (10)). For the stirred vortex simulation $\mu = 6\ \mathrm{s}^{-1}$ and $\sigma = 4$ cm were used (cf. (8)). These are the same values as are represented by the idealized stirred vorticity profile shown in figure 1. In the viscous case, the Ekman time in (13) was taken to be 200 s, a value appropriate for the rotation rate $\Omega = 0.6\ \mathrm{s}^{-1}$. The numerical simulations reproduce the trajectories of the rotating-tank experiments fairly well. Thus, we conclude that the propagation toward the 'northwest' observed in these tank experiments is the barotropic, quasi-geostrophic phenomenon as discussed above. In the inviscid simulations one has $\nu = 0$ and $t_E = \infty$ in (13). The fact that trajectories in the inviscid cases do not deviate much from those of the viscous case, especially at early times, shows that the essential character of the dynamics is inviscid.

There is a qualitative difference between the trajectories of the sink and stirred vortices. The sink vortices in the rotating-tank experiments have a simple smooth arc for a trajectory. The trajectories of the stirred vortices are more complicated. Typically, the path of the stirred vortices has a bend, although the direction remains northwest. Numerical simulations show that the degree of this bend depends on domain size: the larger the domain size, the smoother the trajectory. The portion of the trajectory before the bend is uninfluenced by quadrupling the domain size. This is because in the early part of the motion the annulus of negative vorticity shields the core in such a way that no significant Rossby wave radiation is produced. At later times there is significant Rossby wave radiation, and since the simulations and the experiments are not on an infinite plane, this radiation is not lost and can interfere with the primary vortex. Thus, we find that the later stages of the trajectory are influenced by domain size variations. In some cases, there are significant differences between the trajectories of the simulation and the experiment near the end of the run due to the different boundary conditions. On the other hand, the motion of the sink vortex is strongly affected by domain size variations even at the earliest times, with changes of 50% in the slope for the first 10 s of the trajectory induced by doubling the domain size from 50 to 100 cm. Actually, the smoothness of the sink-vortex trajectories in the tank is a fortuitous result of the size of the initial vortex, for in the numerical simulations we find that doubling the horizontal scale of the vortex produces a bend in the sink-vortex trajectory. A previous study showing trajectories of barotropic laboratory sink vortices over an inclined plan is that of Masuda *et al.* (1990). Their trajectories have sharp bends. We believe the difference in behaviour is due to the relative importance of boundary effects. Judging from the graphs shown by Masuda *et al.*, the horizontal scale of their vortices is much larger relative to the size of the tank than in our experiments. It should be noted that, contrary to our usage, Masuda *et al.* refer to their sink vortices, which do not have vanishing circulation, as isolated vortices.

To illustrate one of the differences between the evolution of the sink and stirred vortices, we show in figure 3 the vorticity fields from the viscous simulations of figure 2. The main feature of the sink evolution (figure 3*a*) is the creation of a dipole pattern which persists with the induced anticyclone remaining to the northeast of the primary cyclone. The stirred vortex starts as an annulus of negative vorticity around a positive core. On the f-plane such vortices are prone to a wavenumber-2 instability (Gent & McWilliams 1986; van Heijst & Kloosterziel 1989; Kloosterziel & van Heijst 1989). As this instability proceeds it deforms the core into an ellipse and causes the negative relative vorticity in the annulus to collect into two satellite anticyclones, as is shown in figure 3*b*. The whole structure rotates about its centre and, due to the β-effect, moves toward the northwest.

Another interesting difference between the sink vortices and the stirred vortices is observed if they are initially dyed. All of the dye initially dispersed near the centre of a laboratory sink vortex is carried along with it, encircling the centre and leaving behind almost no trace in the wake. In contrast, the stirred vortices 'leak', that is, fluid from the outer ring of the vortex is peeled off the core and left behind in a long tendril. The tendril formation is shown in figure 4 in a sequence of nine photographs.

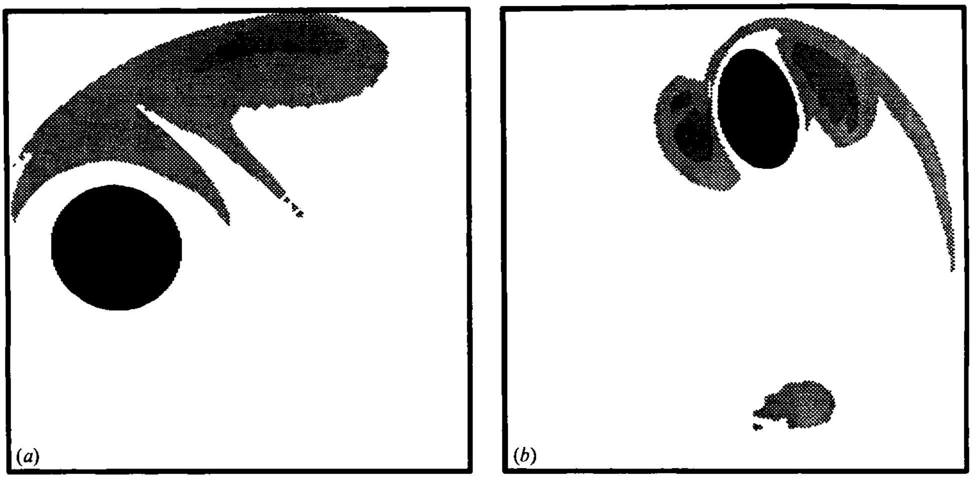

FIGURE 3. Plots of relative vorticity values, showing the difference between sink and stirred vortex evolution. (*a*) Relative vorticity levels of the sink vortex on a β-plane in the viscous numerical simulation at time $t = 40$ s. Black represents positive relative vorticity above the value 0.2 s^{-1}. Negative relative vorticity below $-0.2\ s^{-1}$ is shaded in deepening shades of grey in steps representing magnitude increments of 0.2 s^{-1}. (*b*) Relative vorticity contours of the stirred vortex at time $t = 50$ s in the viscous simulation. The peak vorticity is 1.5 s^{-1}. Positive relative vorticity above 0.4 2^{-1} is shown in black. Negative relative vorticity below $-0.4\ s^{-1}$ is shaded in deepening shades of grey in steps representing increments of magnitude 0.4 s^{-1}. The computational domain size is 50 × 50 cm.

A corresponding sequence of grey-scale plots of passive-scalar evolution from a numerical simulation corresponding to this experiment is shown in figure 5. The simulation used a stirred-vortex profile chosen to approximately match the initial amplitude ($\mu = 5\ s^{-1}$) and horizontal size ($\sigma = 3.5$ cm) of the laboratory vortex whose evolution is shown in figure 4. The resolution employed was 128 × 128 grid points on a domain of size 75 × 75 cm. In the simulation, the passive scalar was initially distributed uniformly over the vortex from the centre out to the point of maximum negative relative vorticity, and from there it rapidly dropped to insignificant levels. The time sequence of the experiment and the simulation shown in figures 4 and 5 is the same. The simulation captures all the features seen in the tank experiment, and the phase correspondence is good except in the last frame (panels *i*). In a numerical study in which an isolated vortex propagates into a field of passive tracer, Holloway *et al.* (1986) showed the formation of a tendril in the dye field. They also showed the formation of the dye patch at the end of the tendril, which is seen in our data as well. We note, however, that a prominent feature in our experiments is the formation of patches or 'blobs' of dye that are left strung along the tendril. These features are not noted in the Holloway *et al.* (1986) simulations. The formation of these blobs occurs at the primary vortex. The blobs are formed by a repetitive process of enfolding and extruding fluid. As discussed above, the stirred vortex undergoes an instability which creates two anticyclones out of the annulus of negative relative vorticity. These form the cores for the first two blobs. As a blob is advected around the core an intrusion of undyed fluid forms, separating it from the main core. When the blob reaches the northeastern side of the core it is pushed against the tendril and is left there as the main core continues to move to the northwest. There is an intrusion of undyed fluid between the tendril and blob, which encircles the core and forms the next bulge in the sequence. A new intrusion of undyed fluid between the blob and the

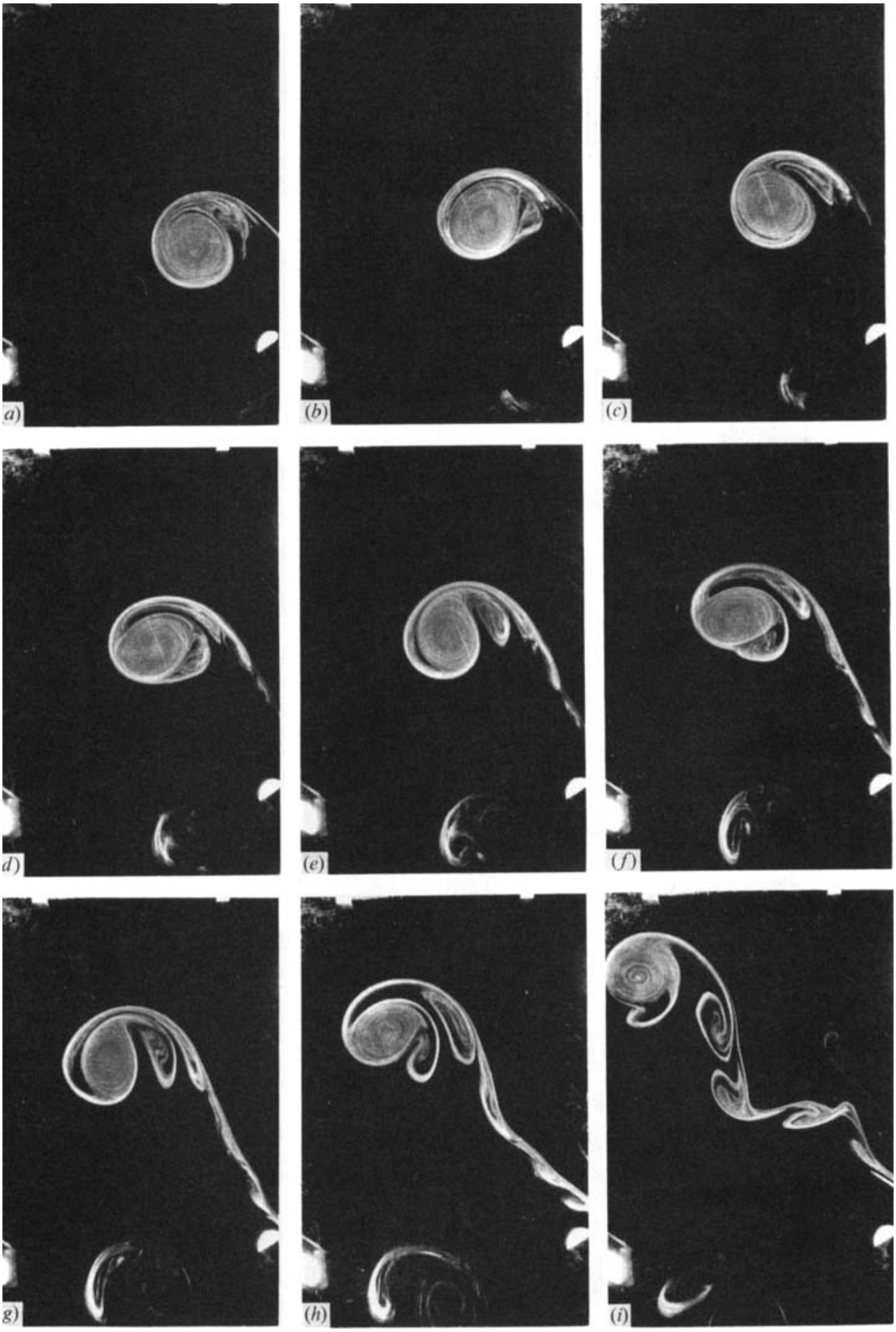

FIGURE 4. Plan-view photographs showing the evolution of the dye concentration in a stirred vortex moving uphill over an inclined plate in the rotating tank. The vortex was created near the deepest part of the fluid layer (at the bottom of the photographs) by stirring in a cylinder with a diameter of 11 cm. All dye was initially contained in the inner cylinder before the release of the vortex. The plate was 50 cm wide by 75 cm long. It was raised 10 cm on the 'north' side (top of the figure). The largest depth of the fluid was 20 cm. The photographs were taken at (*a*) $t = 3.8T$, (*b*) $4.6T$, (*c*) $5.3T$, (*d*) $6.0T$, (*e*) $6.6T$, (*f*) $7.7T$, (*g*) $8.7T$, (*h*) $10.6T$, and (*i*) $14.4T$ after lifting the cylinder, where $T = 10.4$ s is the rotation period of the turntable. The total duration of this experiment was 150 s.

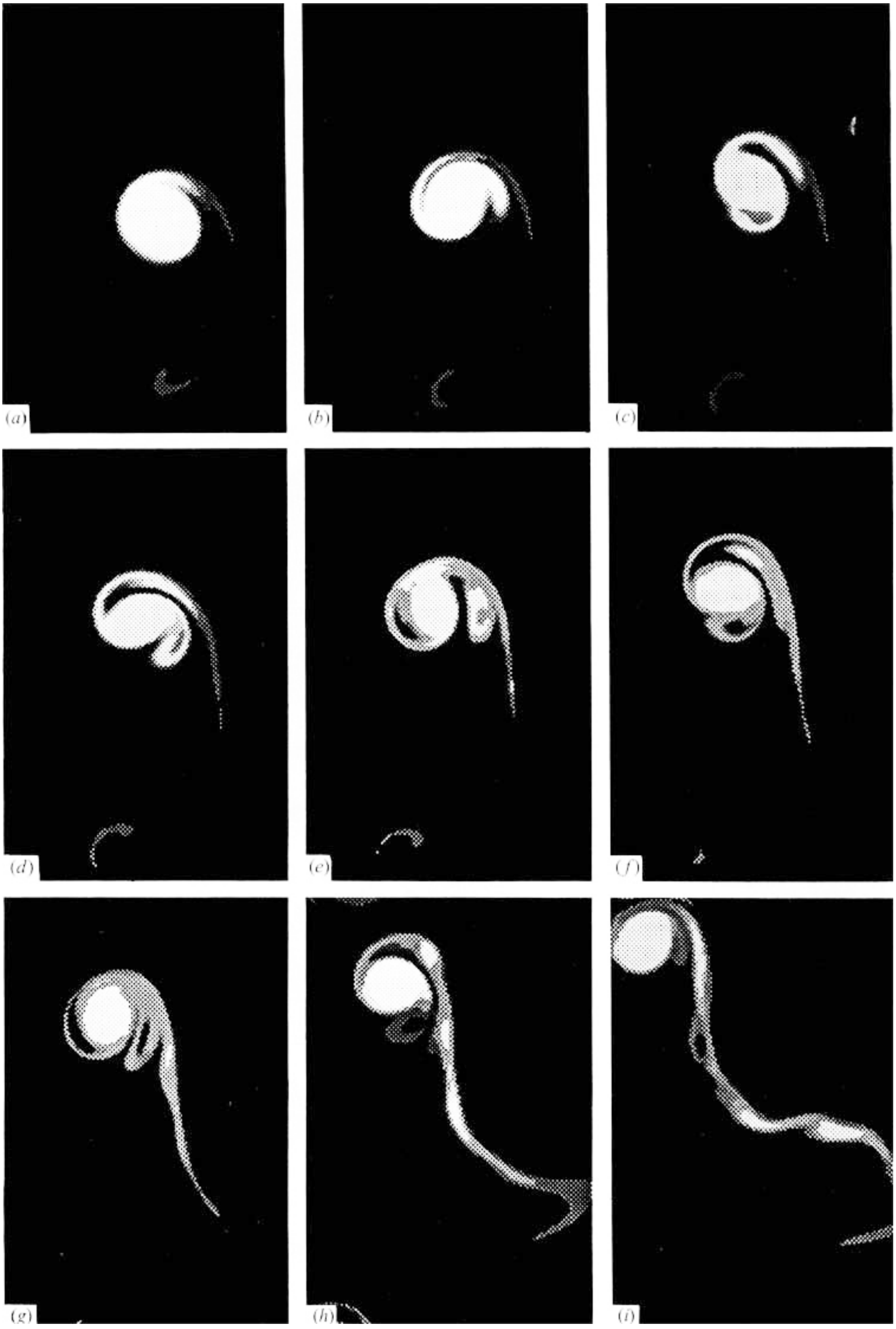

FIGURE 5. Shaded contour plots of the passive scalar field in the numerical simulation corresponding to the rotating-tank experiment shown in figure 4. Undyed fluid is shown in black, while dyed fluid is represented in shades of grey with the lightest representing the highest concentrations. Except for an overall shift due to ambiguity in defining the initial moment in the laboratory experiment, the times corresponding to each panel are exactly the same as in the panels shown in figure 4. The computational domain size is 75 × 75 cm, of which only a portion of 50 × 75 cm is shown.

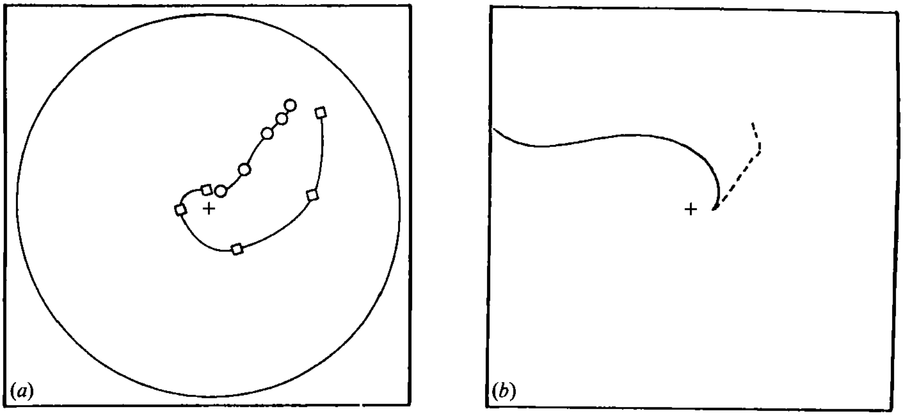

FIGURE 6. Graphs showing the trajectories of cyclones over a conical valley. The rotation rate of the turntable was $\Omega = 1.0\ \mathrm{s}^{-1}$. The depth of the fluid layer in the centre of the tank was 20 cm, and near the tank wall 15 cm. (*a*) Typical sink and stirred vortex trajectories in the laboratory experiments. The data points on the sink vortex trajectory (squares) correspond to times 51, 70, 90, 110, and 132 s after the forcing of the vortex ceased. The data points on the stirred vortex trajectory (circles) correspond to times 6, 24, 44, 67, and 92 s after the vortex was released. The vortices were generated near the centre of the valley (marked +) and then spiralled out. (*b*) Trajectories from numerical simulations of vortices over a conical valley. The duration of the numerical simulation with the sink vortex (solid line) was 54 s whereas the simulation with the stirred vortex (dashed line) lasted 160 s. The final bend in the sink-vortex trajectory is an artifact of the periodic boundary conditions. The computational domain size is 100 × 100 cm.

core eventually moves around the core, and when its head is on the southwest side of the main core, it begins to form another blob. By the time of panel (*g*) of figure 4 several blobs have already been formed. Blob number 3 is the one sandwiched between the tendril and the core. The intrusion between blob 3 and the tendril is connected with blob 4, which is on the west side of the core in panel (*g*). The intrusion between blob 3 and the core will eventually be wrapped up in blob number 5. The proportion of undyed to dyed fluid in successive blobs is an increasing function of time. When each blob is deposited on the tendril, it first appears as an elongated structure, and several may be closely packed on the tendril; later the blobs separate and begin to relax to a more circular form. The result is a string of blobs along the tendril (see panel *i*). This phenomenon was found to be easily reproducible in the laboratory. The ability of the simulations to capture this process allows us to conclude that the underlying mechanism is two-dimensional and quasi-geostrophic. Furthermore, this process also occurs in inviscid simulations, which shows that explicit viscosity is not essential here.

3.2. *Conical-valley experiments*

A series of laboratory experiments was performed in which cyclones were created on the slope of a conical valley. The bottom of the rotating tank was covered entirely by an inverted right-circular cone. The maximum depth was approximately 20 cm at the centre, sloping to 15 cm at the tank wall. The rule of propagation to the local northwest predicts that a cyclone spirals up and out of the valley in a cyclonic sense. Trajectories of a typical sink vortex and a typical stirred vortex are shown in figure 6(*a*). The data points for the sink (stirred) vortices are indicated by squares (circles). Both vortices were created near the centre of the valley and move outward in time. Note that the stirred vortex shows a nearly radial trajectory, which is locally 'northward', whereas the spiral of the sink vortices indicates a more northwestward

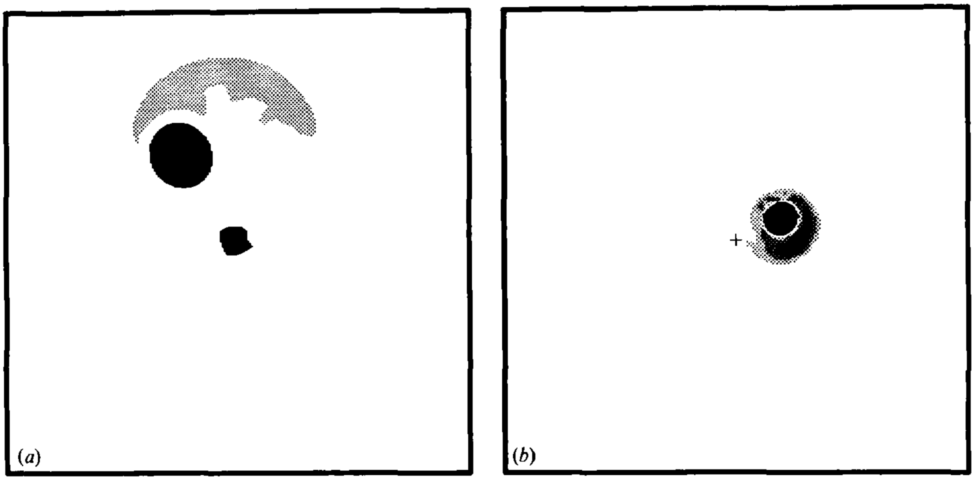

FIGURE 7. Graphs showing relative vorticity levels at time $t = 30$ s in the viscous numerical simulation of (*a*) sink and (*b*) stirred vortices over a conical valley. The centre of the valley is marked + in each plot (not visible in *a* but at the same position as in *b*). The computational domain size is 100 × 100 cm. In (*a*), the sink vortex creates a secondary cyclone over the centre of the valley as discussed in the text. The small secondary cyclone at the centre has an amplitude of about 10% of that of the primary vortex. Positive relative vorticity above the value 0.2 s^{-1} is coloured black. Negative relative vorticity below the value of $-0.2\ \mathrm{s}^{-1}$ is indicated by light grey. In (*b*), the core of this stirred vortex has a maximum vorticity amplitude of 3.2 s^{-1}. Positive relative vorticity above the value 0.1 s^{-1} is coloured black. Negative relative vorticity is shaded in deepening shades of grey in steps representing increments of magnitude 0.1 s^{-1}.

angle locally with the gradient of topography. This observation is qualitatively in accordance with the results of § 3.1, where the stirred vortices on a β-plane were seen to have a larger northward component in their overall motion than the sink vortices. These experiments were performed with the high rotation rate $\Omega = 1\ \mathrm{s}^{-1}$; others performed with the lower rate $\Omega = 0.6\ \mathrm{s}^{-1}$ showed qualitatively similar results.

In figure 6(*b*), we show the results of viscous numerical simulations with conditions corresponding to the experiments shown in figure 6(*a*). For the sink vortex the initial parameters used are $\sigma = 3$ cm and $\mu = 5\ \mathrm{s}^{-1}$, and for the stirred vortex $\sigma = 2.5$ cm and $\mu = 3.3\ \mathrm{s}^{-1}$. The initial position of the vortices in the simulation was 5 cm from the centre of the valley. The qualitative difference between the paths of the isolated stirred vortices and the sink vortices seen in the experiments appears in the simulations too. For the sink vortex the cyclonic sense of the spiral is clear, while the stirred vortex tends to follow a more radial path outward. A series of simulations was performed which revealed that these trajectories are very sensitive to changes in the initial amplitude, size and, in particular, position of the vortices. Thus obtaining a good quantitative match here would require very precise parameter tuning beyond what is warranted for present purposes. In the simulation of the sink vortex, the final bend in the trajectory before the vortex leaves the computational domain is an artifact of the periodicity of the topography, as has been verified by increasing the domain size. Even in the tank we must expect that, as the wall is approached, the details of the motion are strongly affected by the boundaries, especially in the case of the sink vortices. Finally, we note that the trajectories were not qualitatively different in the inviscid simulations.

Figure 7 shows the relative vorticity fields at time $t = 30$ s of the simulations depicted in figure 6(*b*). Figure 7(*a*) shows the dipolar structure which forms as the

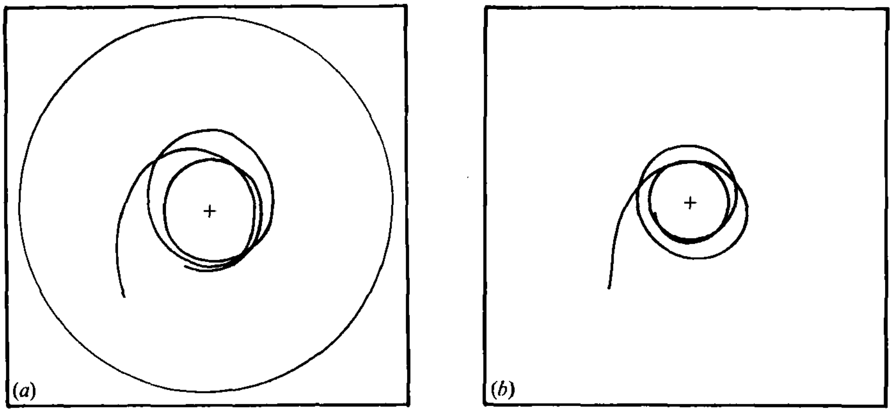

FIGURE 8. Graphs showing the trajectories of sink vortices over a conical hill as observed (*a*) in the laboratory and (*b*) in a viscous numerical simulation. The laboratory vortex was created by siphoning 3.5 l of water in 13 s at the bottom of the tank (on the sloping hill). The rotation rate of the table was $\Omega = 0.6\ \mathrm{s}^{-1}$, the height of the conical hill 5 cm, and the average water depth, halfway between the centre of the tank and the tank wall, was $D = 17.5$ cm. The position of the vortex was determined from streakline photographs every 15 s. The entire trajectory of the laboratory vortex shown in (*a*) covers a period of 280 s. In (*b*) the duration of the numerical experiment was 300 s. The computational domain size is 100 × 100 cm. Further details are given in the text. The peak of the hill is marked +.

sink vortex moves away from the centre. This structure is in accord with our local view of the propagation. However, a small cyclonic vortex is also created directly over the centre of the tank. This can be understood in terms of the theory of large-scale flow over topography (see Huppert & Bryan 1976). An impulsively started, large-scale flow over a topographic valley creates a stable cyclone directly above the centre of the valley. This occurs because quiescent fluid advected over the centre must develop positive relative vorticity in order to maintain its initial zero potential vorticity. This secondary cyclonic flow can be maintained against viscous decay as long as the large-scale forcing continues to operate, and the primary sink vortex can act as the large-scale flow in this mechanism (cf. Carnevale *et al.* 1988). The presence of the fixed secondary cyclone in the centre of the tank can only increase the local westward speed, thus resulting in a tighter spiral than would otherwise result from the local northwest propagation mechanism. Finally, in figure 7(*b*) we see that the stirred vortex does not induce a cyclone over the centre of the valley. This is due to the isolated character of the stirred vortex.

3.3 *Conical-hill experiments*

Another series of experiments was performed with the bottom of the tank covered by a conical hill. In this case, the shallowest point was 15 cm deep at the centre of the tank, while the deepest section was 20 cm deep along the tank wall. The local northwest rule implies that a cyclone will spiral toward the top of the hill in an anticyclonic sense.

An example of a trajectory of a sink vortex created far from the peak of the hill in the tank is shown in figure 8(*a*). The initial tendency is, indeed, an anticyclonic spiral in toward the centre of the tank. However, as the vortex approaches the centre, the motion is transformed into a looping motion about the centre, which is not in agreement with the local northwest propagation rule. Owing to the overlap of loops, we have not shown data points on this trajectory. The duration of the trajectory is 280 s during which the vortex executes about three full loops around the centre of the hill. By varying the strength and initial position of the vortex, we have observed a variety of trajectories, all of which have an anticyclonic looping around the peak in common but with varying degree of initial inward motion. In fact, vortices created close to the top merely execute a circular motion from the outset.

In figure 8(*b*) the result from the viscous simulation of the experiment of figure 8(*a*) is shown. The Ekman time (200 s) for the viscous simulation was based on the average depth $D = 17.5$ cm, with Ω and ν as in § 3.1 and $\{\mu, \sigma\} = \{5\ \mathrm{s}^{-1}, 3\ \mathrm{cm}\}$. The duration of the simulation was 300 s. The simulation uses topography which corresponds to the shape of the cone. The corresponding inviscid simulation gives qualitatively the same behaviour as shown in figure 8(*b*), except with a higher number of loops.

The failure of the local northwest rule to predict the looping motion implies that some non-local mechanisms must come into play as the vortex approaches the peak. This is not entirely surprising. Our rule was formulated under the assumption that the characteristic lateral scale of the vortex is small compared to the scale of the horizontal gradients of topography. However, near the peak of the topography the horizontal topographic scales become comparable if not smaller than that of the vortex. The degree to which the vortex climbs the hill and the complexity of the orbit depend on the size, strength, and position of the initial vortex. This has been examined systematically in a series of numerical experiments. The motion is more inward initially if the horizontal scale of the sink vortex is small. Sink vortices placed farther from the centre of the cone have a larger inward component to the initial motion than when placed near the centre. If sufficiently wide or sufficiently close to the peak of the topography, they have nearly circular trajectories, which agrees with the rotating-tank experiments. The motion close to the peak can be understood in terms of the theory of large-scale flow over topography as discussed in the previous section. Large-scale flow over a hill produces an anticyclone over the peak. In some simulations the creation of a separate patch of negative vorticity over the peak was clearly observed. The vortices that execute nearly circular trajectories have created a negative vorticity anomaly over the peak, which blocks further advancement of the primary vortex up the cone and carries the primary in an anticyclonic manner about the peak. Modification of the topography shows that vortices approach closer to the centre of a cone if the peak is removed. Finally we note that stirred vortices on the conical hill show trajectories that are almost directly inward towards the peak, that is, with no looping motion. This is because the stirred vortex is an isolated structure, which, from a distance, cannot induce an anticyclone over the peak.

3.4. *Effects of free-surface slope*

As noted in the introduction, the variation of depth due to the free-surface slope is small compared to the topographic gradients used in the previous sections. However, when considering experiments over a flat bottom the effect of the free surface proves surprisingly important even at the low rotation rates used in the experiments. In a series of experiments, cyclones were followed as they evolved over a flat bottom. Actually, taking account of the parabolic shape of the free surface, this can be thought of as motion over a parabolic hill. In the laboratory experiments, the cyclones were found to spiral in towards the centre of the tank, making excursions of length comparable to the tank diameter in one to two Ekman periods. This is illustrated in the first two panels of figure 9. The rotation rate in these experiments

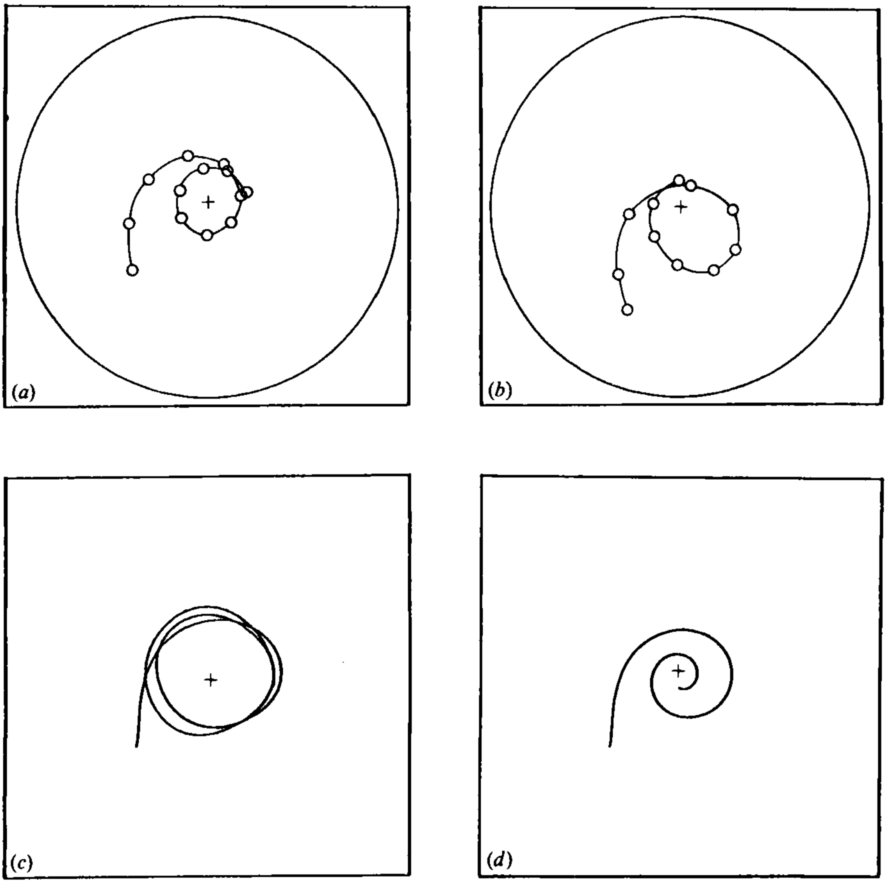

FIGURE 9. Graphs showing the trajectories of cyclonic vortices in a rotating tank with a free surface and no bottom topography: (*a*) and (*b*) show the trajectories of two typical sink vortices in the laboratory experiments. The mean water depth was $D = 20$ cm and the rotation rate was $\Omega = 1.0\ \mathrm{s}^{-1}$. In both cases, the inward part of the motion lasted for about 100–120 s before the looping motion began. The vortex of (*a*) was created by siphoning 3.2 l of water in 13 s from the tank and that of (*b*) was created in a similar manner, but with 2.45 l in 25 s. The data points (circles) represent about half of the points used to plot these trajectories. The points shown in (*a*) correspond to the times 40, 70, 100, 130, 160, 190, 220, 250, 290, 330, 370, 410, and 450 s after the forcing was stopped, and in (*b*) to times 17, 50, 30, 110, 140, 170, 220, 230, 260, 290, and 325 s. Panels (*c*) and (*d*) show the trajectories of the motion of a sink vortex under a free surface in inviscid and viscous simulations respectively. The Ekman time (175 s), vorticity diffusion, and 'free-surface topography' were based on a molecular viscosity of 0.013 $\mathrm{cm}^2\ \mathrm{s}^{-1}$ and the values of D and Ω given above. The duration of these numerical simulations was 500 s. The computational domain size is 100×100 cm. The centre of the domain is marked +.

was $\Omega = 1.0\ \mathrm{s}^{-1}$ which results in a parabolic curvature of the surface with an overall depth variation of about 1 cm. The vortices in these experiments were created by the suction method. The duration of the experiments was 5–7 min. It is important to note that in a constant-depth fluid (under a rigid lid) no such translationary motion is observed. In figure 9(c, *d*) we show the respective trajectories of an inviscid and viscous simulation of a sink vortex under a free surface. The duration of the trajectories shown was 500 s. The number of loops in the inviscid simulation (figure 9*c*) is almost double that found in the experiments. If viscosity is added to the simulations the number of loops is reduced, but instead of staying away from the centre of the domain, the vortex continues to spiral inwards (figure 9*d*). Some fine tuning of initial conditions, boundary conditions and viscosity is necessary to bring the simulations into better agreement with the experiments; however, the essential feature of the inward spiral and the gross characteristics of the trajectory are captured by these simulations. Numerical simulation and laboratory experiments (Kloosterziel & van Heijst 1991) show that stirred vortices under the free-surface slope also move in toward the centre.

These results thus show that in the absence of stronger topographic effects, the free-surface slope can cause a significant motion of a vortex in the rotating tank. This is especially surprising in the light of dimensional arguments (cf. Flierl, Stern & Whitehead 1983) which would suggest that the free-surface effect is small. Specifically, if we form a dimensionless number from σ, μ, and β_{eff} is computed from the largest free-surface slope, we find

$$\beta_{\text{eff}}\, \sigma/\mu \leqslant 0.003. \tag{16}$$

Naively, this number would seem to represent a ratio of the β-effect to pure advection; however, its meaning cannot be that simple since for a radially symmetric vortex the purely advective terms cancel exactly in the equation of motion. In fact, the propagation speed of the vortex reaches a value of about 0.5 cm s^{-1}, which is very significant for experiments in a tank of 50 cm radius and a spin-down time of 200 s. We suggest that this effect holds the answer to puzzles in past experimental work. Specifically, we note the strong discrepancy between theory and experiment pointed out by Griffiths & Hopfinger (1987) in the experimental verification of vortex mergers. Theory suggests no difference in the criteria for merger between cyclones and anticyclones. Griffiths & Hopfinger, however, have shown that in rotating-tank experiments with a free surface anticyclones obey the theory within experimental error, while the cyclones merge far more readily than the theory would allow. We speculate that the asymmetry is due to the free-surface β-effect, which tends to bring the cyclones together at the tank centre, permitting a merger which otherwise would not have occurred.

4. Discussion

Based on our numerical simulations and rotating-tank experiments, we conclude that the tendency for a cyclone to propagate to the northwest on a β-plane translates into a simple rule of thumb for propagation of cyclones over topography or through layer-thickness variations in general. Thus we expect cyclones to move toward the local northwest as defined by the local gradients of topography – by symmetry anticyclones will move to the local southwest. For a cyclone on a hill, this implies an anticyclonic spiral toward the top of the hill. For cyclones in a valley, it implies a cyclonic spiral climbing up out of the valley. The underlying physical mechanism here is inviscid vortex tube stretching and relies on nonlinear advection. These results also offer an explanation for the observed inward motion of cyclones created in a rotating tank with a free surface. We have found that viscous effects, specifically Ekman drag and horizontal vorticity diffusion, of the magnitude acting in the rotating-tank experiments, do not obscure the basic inviscid nonlinear tendency. Furthermore, by direct comparison we have shown that these results are valid for both isolated and non-isolated vortices.

Simulations by McWilliams & Flierl (1979) and Mied & Lindemann (1979) demonstrate that the β-plane effect also causes translation of stratified vortices. If a given stratified eddy has a strong barotropic component, we speculate that a bottom slope may produce translation in the sense described above. In this regard, it is interesting to consider the comments of Mory, Stern & Griffiths (1987). They suggested that the observed propagation to the local northwest of lenses over a sloping bottom is a viscous effect driven by bottom friction; however, they did note "Part of the northward movement of the lens might also be attributed to weak radiation of Rossby waves (McWilliams & Flierl 1979) or other inertial wake effects that cause the energy of the cyclone vortex to decrease....We were not able to provide a quantitative estimate of this second mechanism, but our analysis of the experiment indicates that it is at most as important as the effect of Ekman friction." So further work on sorting the relative effects of viscosity and nonlinear radiation is needed, but the simple vortex stretching mechanisms at work on a β-plane may also translate into simple rules for the propagation of baroclinic vortices over topography.

Finally, we note that there is something of a paradox posed by this mechanism which has cyclones climb hills and anticyclones descend into valleys. Previous work on flow over topography emphasized that the vorticity field should become anticorrelated with the topography, whereas the local northwest propagation rule tends to produce vorticity fields that are correlated with the topography. We have already mentioned that large-scale flow over topography creates an anticyclone over the topographic peak, but there is no contradiction there since the issue is one of scale, with the local northwest rule holding only when the horizontal scale of the vortex is small compared to that of the horizontal variations of topography. It is somewhat more interesting to consider the results of nonlinear stability theory and statistical theory. Based on considerations of the energy and potential enstrophy invariants of the flow, both of these theories predict states with relative vorticity anticorrelated with topography (cf. Bretherton & Haidvogel 1976; Salmon, Holloway & Hendershott 1976; Herring 1977; Carnevale & Frederiksen 1987). Thus, at first, the existence of a mechanism which tends to result in positive vortices over positive topography may appear contradictory. However, as pointed out in Carnevale & Frederiksen (1987), both the nonlinear stability and the statistical analysis of the flow over topography based only on energy and enstrophy must miss effects which rely on the pointwise conservation of potential vorticity. Hence, one must generalize the equilibrium distribution to contain more information than just energy and enstrophy conservation in order to capture such effects. There is no contradiction with statistical theory if one realizes that energy and enstrophy conservation alone cannot properly define the stationary ensemble. Similarly, as originally pointed out by Bretherton & Haidvogel (1978), the theory of nonlinear stability of flow over topography allows for more complicated relations between stream function and topography with the stability of such states relying on conservation of vorticity invariants other than enstrophy.

This research has been supported in part by National Science Foundation grants OCE 89-11858 and ATM 8914004, by the Office of Naval Research grant N00014-89-J-1155, by ONR/DARPA under the University Research Initiative Program no. N0014-86-K-0758, and by the working group on Meteorology and Physical Oceanography (MFO) of the Netherlands Organization of Scientific Research (NWO). The numerical simulations were performed at the San Diego Supercomputer Center. The rotating tank experiments were performed at the University of Utrecht.

REFERENCES

Adem, J. 1956 A series solution for the barotropic vorticity equation and its application in the study of atmospheric vortices. *Tellus* VIII, 364–372.

Bjerkness, J. & Holmboe, J. 1944 On the theory of cyclones. *J. Mete.* **1**, 1–22.

Bretherton, F. P. & Haidvogel, D. B. 1976 Two-dimensional turbulence above topography. *J. Fluid Mech.* **78**, 129–154.

Carnevale, G. F. & Frederiksen, J. S. 1987 Nonlinear stability and statistical mechanics of flow over topography. *J. Fluid Mech.* **175**, 157–181.

Carnevale, G. F., Vallis, G. K., Purini, R. & Briscolini, M. 1988 Propagation of barotropic modons over topography. *Geophys. Astrophys. Fluid Dyn.* **41**, 45–101.

Carr, L. E. & Williams, R. T. 1989 Barotropic vortex stability to perturbations from axisymmetry. *J. Atmos. Sci.* **46**, 3177–3191.

Chan, J. C. L. & Williams, R. T. 1987 Analytical and numerical studies of the beta-effect in tropical cyclone motion. Part I: Zero mean flow. *J. Atmos. Sci.* **44**, 1257–1265.

Firing, E. & Beardsley, R. C. 1976 The behavior of a barotropic eddy on a β-plane. *J. Phys. Oceanogr.* **6**, 57–65.

Flierl, G. R. 1977 The application of linear quasi-geostrophic dynamics to gulf stream rings. *J. Phys. Oceanogr.* **7**, 365–379.

Flierl, G. R., Stern, M. E. & Whitehead, J. A. 1983 The physical significance of modons: laboratory experiments and general integral constraints. *Dyn. Atmos. Oceans* **7**, 233–263.

Gent, P. R. & McWilliams, J. C. 1986 The instability of barotropic circular vortices. *Geophys. Astrophys. Fluid Dyn.* **35**, 209–233.

Griffiths, R. W. & Hopfinger, E. J. 1987 Coalescing of geostrophic vortices. *J. Fluid Mech.* **178**, 73–97.

Heijst, G. J. F. van & Kloosterziel, R. C. 1989 Tripolar vortices in a rotating fluid. *Nature* **338**, 569–571.

Herring, J. R. 1977 On the statistical theory of two-dimensional topographic turbulence. *J. Atmos. Sci.* **34**, 1731–1750.

Holloway, G., Riser, D. C. & Ramsden, D. 1986 Tracer anomaly evolution in the flow field of an isolated eddy. *Dyn. Atmos. Oceans* **10**, 165–184.

Holton, J. R. 1979 *An Introduction to Dynamic Meteorology*. Academic.

Huppert, H. E. & Bryan, K. 1976 Topographically generated eddies. *Deep-Sea Res.* **23**, 655–679.

Kloosterziel, R. C. 1990 On the large-time asymptotics of the diffusion equation on infinite domains. *J. Engng Maths* **24**, 213–236.

Kloosterziel, R. C. & Heijst, G. J. F. van 1989 On tripolar vortices. In *Mesoscale/Synoptic coherent Structures in Geophysical Turbulence* (ed.) J. C. J. Nihoul, pp. 609–625. Elsevier.

Kloosterziel. R. C. & Heijst, G. J. F. van 1991 An experimental study of unstable barotropic vortices in a rotating fluid. *J. Fluid Mech.* **223**, 1–24.

Masuda, A., Marubayashi, K.. & Ishibashi, M. 1990 A laboratory experiment and numerical simulation of an isolated barotropic eddy in a basin with topographic β *J. Fluid Mech.* **213**, 641–659.

McWilliams, J. C. & Flierl, G. R. 1979 On the evolution of isolated, nonlinear vortices. *J. Phys. Oceanogr.* **9**, 1155–1182.

McWilliams, J. C., Gent, P. R. & Norton, N. J. 1986 The evolution of balanced, low-mode vortices on the β-plane. *J. Phys. Oceanogr.* **16**, 838–855.

Mied, R. P. & Lindemann, G. R. 1979 The propagation and evolution of cyclonic Gulf Stream rings. *J. Phys. Oceanogr.* **9**, 1183–1206.

Mory, M., Stern, M. E. & Griffiths, R. W. 1987 Coherent baroclinic eddies on a sloping bottom. *J. Fluid Mech.* **183**, 45–62.

Patterson, G. S. & Orszag, S. A. 1972 Spectral calculations of isotropic turbulence, efficient removal of aliasing interactions. *Phys. Fluids* **14**, 2538–2541.

Pedlosky, J. 1979 *Geophysical Fluid Dynamics*. Springer.

Rossby, C. G. 1948 On displacements and intensity changes of atmospheric vortices. *J. Mar. Res.* VII, 175–187.

SALMON, R., HOLLOWAY, G. & HENDERSHOTT, M. C. 1976 The equilibrium statistical mechanics of simple quasi-geostrophic models. *J. Fluid Mech.* **75**, 691–703.

TAKEMATSU, M. & KITA, T. 1988 The behavior of an isolated free eddy in a rotating fluid: Laboratory experiment. *Fluid Dyn. Res.* **3**, 400–406.

TOJO, S. 1953 The dynamics of a vortex embedded in a constant zonal current. *J. Met.* **10**, 175–178.

WILLOUGHBY, H. E. 1988 Linear motion of a shallow-water, barotropic vortex. *J. Atmos. Sci.* **45**, 1906–1928.